ADVANCED MATERIALS
www.advmat.de

Spontaneous Supercrystal Formation During a Strain-Engineered Metal–Insulator Transition

Oleg Yu. Gorobtsov, Ludi Miao, Ziming Shao, Yueze Tan, Noah Schnitzer, Berit Hansen Goodge, Jacob Ruf, Daniel Weinstock, Mathew Cherukara, Martin Victor Holt, Hari Nair, Long-Qing Chen, Lena Fitting Kourkoutis, Darrell G. Schlom, Kyle M. Shen, and Andrej Singer*

Mott metal–insulator transitions possess electronic, magnetic, and structural degrees of freedom promising next-generation energy-efficient electronics. A previously unknown, hierarchically ordered, and anisotropic supercrystal state is reported and its intrinsic formation characterized in-situ during a Mott transition in a Ca_2RuO_4 thin film. Machine learning-assisted X-ray nanodiffraction together with cryogenic electron microscopy reveal multi-scale periodic domain formation at and below the film transition temperature ($T_{Film} \approx 200$–250 K) and a separate anisotropic spatial structure at and above T_{Film}. Local resistivity measurements imply an intrinsic coupling of the supercrystal orientation to the material's anisotropic conductivity. These findings add a new degree of complexity to the physical understanding of Mott transitions, opening opportunities for designing materials with tunable electronic properties.

1. Introduction

The structural complexity of artificial nanomaterials challenges empirical understanding yet provides unique opportunities for controllable emergent functional properties. Supercrystals – structures with coexisting spatial periodicities larger than the atomic unit cell – present an intriguing opportunity to access new properties in the field of nanomaterials. Recently, metastable supercrystals were discovered to arise in an artificial $PbTiO_3/SrTiO_3$ superlattice through a nonequilibrium transition.[1] In 2D materials, moiré patterns can be interpreted as 2D supercrystals, showcasing an additional few-nanometer-large periodic scattering potential for charge carriers.[2,3] Of particular interest for technology are potential applications in mottronics – electronics relying on Mott insulators.[4] The range of control possibilities in Mott insulators already makes them attractive for diverse applications such as memory elements,[5] optical switches,[6] and brain emulation.[7] In Mott insulators with a structurally driven metal–insulator transition (MIT), introducing periodic structural distortions at the nanoscale could provide a particularly potent control lever over the energy balance between competing ground states.

O. Y. Gorobtsov, Z. Shao, N. Schnitzer, J. Ruf, D. Weinstock†, H. Nair, D. G. Schlom, A. Singer
Department of Materials Science and Engineering
Cornell University
Ithaca, NY 14853, USA
E-mail: gorobtsov@cornell.edu

L. Miao, K. M. Shen
Department of Physics
Cornell University
Ithaca, NY 14853, USA

Y. Tan, L.-Q. Chen
Department of Materials Science and Engineering
Pennsylvania State University
University Park, PA 16802, USA

B. H. Goodge, L. F. Kourkoutis†
School of Applied and Engineering Physics
Cornell University
Ithaca, NY 14853, USA

B. H. Goodge, L. F. Kourkoutis†, D. G. Schlom, K. M. Shen
Kavli Institute at Cornell for Nanoscale Science
Cornell University
Ithaca, NY 14853, USA

B. H. Goodge
Max Planck Institute for Chemical Physics of Solids
01187 Dresden, Germany

M. Cherukara, M. V. Holt
Center for Nanoscale Materials
Argonne National Laboratory
Argonne, IL 60439, USA

M. Cherukara
Advanced Photon Source
Argonne National Laboratory
Argonne, IL 60439, USA

D. G. Schlom
Leibniz-Institut für Kristallzüchtung
Max-Born-Straße 2, 12489 Berlin, Germany

The ORCID identification number(s) for the author(s) of this article can be found under https://doi.org/10.1002/adma.202403873

†Authors deceased

DOI: 10.1002/adma.202403873

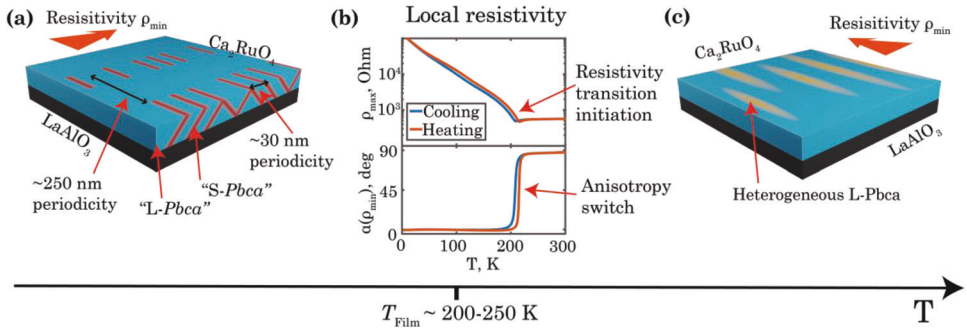

Figure 1. Schematic of the supercrystal structure and properties in Ca_2RuO_4. a) Schematic representation consistent with x-ray data of the supercrystal structure below MIT temperature. Apart from the atomic, two periodicities are present: the ≈30 nm periodicity found in the cross-cut of the film, corresponding to a fine herringbone domain-like heterogeneity, and the ≈250 nm periodicity found in the film plane. b) Local resistivity of the film (top) and orientation of the easy axis in resistivity (bottom) as a function of temperature. c) Schematic representation of the anisotropic structure above MIT temperature, where the L-Pbca possesses an additional heterogeneity.

Calcium ruthenate, Ca_2RuO_4, is a Mott insulator with a structurally driven MIT between an insulating *S-Pbca* (bulk crystal lattice parameters at 295 K: a = 5.41 Å; b = 5.49 Å; c = 11.96 Å) and a metallic *L-Pbca* (bulk crystal lattice parameters at 400 K: a = 5.36 Å; b = 5.35 Å; c = 12.26 Å) orthorhombic phases,[8,9] where strain directly influences the transition.[10,11] Bulk Ca_2RuO_4 undergoes MIT at a critical temperature of T_{Bulk} = 357 K,[12] which can be lowered by biaxial compressive strain in thin films to T_{Film} = 230 K[13] or triggered by a surprisingly low electric field,[14] making it an attractive candidate for beyond-CMOS electronic devices. Optical, x-ray, and neutron studies suggested the presence of a surface nanotexture during the current-induced MIT in bulk Ca_2RuO_4[15–17] connected to anistropic strain between structural phases. The question then is whether an organized nanotexture can be induced by stress in the thin films to manipulate electronic properties.

Here, we report an anisotropic, hierarchical nanotexture composed of coexisting structural phases induced via epitaxial strain, confinement, and cooling in a 34 nm thick Ca_2RuO_4 film grown on $LaAlO_3$. We observe at least three different length scales, demonstrating a high degree of complexity arising from relative simplicity of the unit cell. The temperature-induced modulation of the supercrystal anisotropy modulates the directional electric properties. The structure and behavior of the induced supercrystal are summarized in **Figure 1**. Below the MIT temperature, an anisotropic multiperiodic structure forms with periods of 30 and 250 nm (Figure 1a). The 250 nm structure correlates with anisotropy of microscopic local resistivity (Figure 1b). As we heat the film above the MIT temperature, the 30 nm periodicity vanishes, and a different anisotropic structure at 250 nm arises with a 90° in-plane rotation, coincident with a rotation of anisotropic resistivity direction by 90° (Figure 1c).

2. In Situ Superstructure Observation

We have found the nanoscale heterogeneity in the Ca_2RuO_4 thin films in situ during the transition by combining methods tailored explicitly to studies of lattice distortions in thin crystalline films. Namely, conventional X-ray diffraction (XRD), X-ray Bragg nanodiffraction, and cryogenic scanning transmission electron microscopy (cryo-STEM). The advantages and disadvantages of the respective methods make them well-suited for studies of a domain hierarchy. Nanodiffraction provides non-invasive measurements of comparatively large (several micrometers across) areas, with continuous temperature control, but the resolution was limited to ≈30 nm. Cryo-STEM provided atomic-scale resolution, but is limited to small (tens to hundreds of nanometers) areas, is more invasive, and is only now being extended to arbitrary cryogenic temperatures.[18,19] X-ray nanodiffraction and cryo-STEM are therefore complementary techniques that provide information on different length scales and in different geometry ("top", or in-plane, view in X-ray nanodiffraction, "side", or cross-cut, view in cryo-STEM). The Bragg diffraction from the film illuminated by a focused X-ray, schematically shown in **Figure 2a** depends on the local crystal structure, that is, regions in the film with significantly different lattice periods along the probed wavevector manifest as separate Bragg peaks on the detector. We performed scanning X-ray nanodiffraction on a 5 × 5 µm region of the film, collecting spatial maps of the same region at different temperatures (Figure 2a). The technique employs a raster-scan of a coherent X-ray beam focused down to 30 nm to resolve the crystal structure, structural phase, and strain distribution in thin (typically < 100 nm) films.[20] The scattering volume for a 30 nm focused X-ray beam is orders of magnitude smaller than in conventional XRD, significantly limiting the amount of signal (Figure 2b).

In bulk Ca_2RuO_4 crystals, the lattice period in the [001] direction in the low-temperature and high-temperature phases differs by ≈2–3%, and XRD shows two distinct Bragg peaks during the discontinuous phase transformation.[12,17] In the strained thin film, we found an intricate diffraction pattern instead of clearly separable Bragg peaks corresponding to different phases. Apart from the circular features introduced by the focusing of the x-ray beam, the pattern shown in the experimental sketch (Figure 2a) shows a strong peak in the center and a weaker diagonal streak across the detector (see Figure S5, Supporting Information for magnified average diffraction pattern). Synchrotron beamlines dedicated to nanoscale focusing of hard x-rays ensure a high degree of coherence to achieve the highest real-space spatial resolution but produce complex far-field diffraction patterns that uniquely encode any crystallographic perturbations within the illuminated nano-volume into "speckled" intensity variations

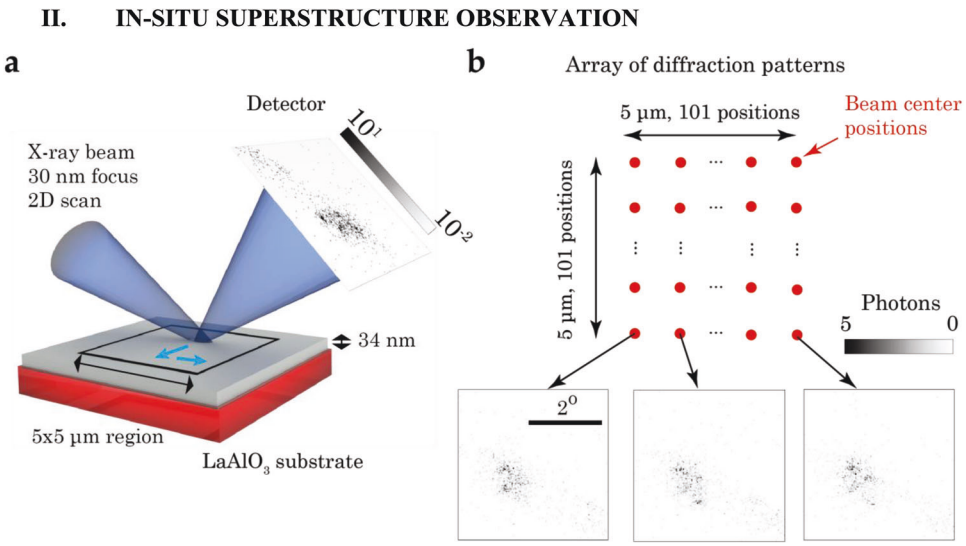

Figure 2. X-ray nanodiffraction scheme. a) Geometry of the nanodiffraction experiment. X-ray beam focused down to ≈30 nm size scans a region of the Ca_2RuO_4 film at different temperatures, with individual diffraction patterns around a (008) Bragg reflection recorded on the detector. b) The result is an array of 2D diffraction patterns corresponding to different positions, with signals in individual pixels on the order of several photons. Example diffraction patterns are for the sample at 250 K.

at the detector.[21] Although the patterns are extremely difficult to predict for non-ideal crystals and cause artifacts in purely intensity-based analysis methods, the detected complex wavefield forms an exact one-to-one relationship with its formative structure. We exploit this one-to-one relationship within the context of a scalable domain structure, which ensures that a properly sampled spatial map will produce far-field diffraction patterns with separable regions based on the re-occurrence of self-similar beam/domain interactions within the map, allowing classification of the regions without the need to deduce the local beam-sample interaction.

The complexity of the diffraction data and low signal make the manual decoupling of different features in reciprocal space challenging. Therefore, we applied unsupervised machine learning (classification) to differentiate between different regions of the diffraction pattern based on their corresponding structure maps of the film.[22] As a first step, we used principal component analysis (PCA)[23–25] to understand the structure of the data and estimate the number of classes. More specifically, for the whole array of 2D diffraction patterns produced in a raster scan, we found the first 3 principal components in the real (film) space showing the most change in the intensity at different positions on the detector (see Figure S6, Supporting Information). That is, in computational terms,each pixel on the detector wasan "observation" and intensities in each position on the film were "features". As an example, if the intensity in two different pixels behaves similarly when scanning across the film, they have similar coordinates along the principal components (see Experimental Section: Machine Learning for more details). While PCA provided visual guidance, to classify the data, we used an unsupervised learning algorithm – k-means clustering K-means clustering is a converging vector quantization algorithm for the classification of observations (detector pixels in our case) based on the similarity of features (corresponding intensity maps on the film).[26] We follow the procedure in[22] (see also Methods: machine learning for more specific parameters), which involved determining positions of k centroids (cluster centers) in the same space as described for PCA (i.e., the space with the number of dimensions being the number of points probed of the film, with coordinates being intensity), with every pixel on the detector assigned a class/cluster based on which centroid is the closest to it. We classified regions of diffraction patterns at different temperatures separately, because the domain patterns, especially intrinsic, evolve through the MIT. **Figure 3b** shows the classification results for diffraction patterns measured on the heating branch at a fixed temperature of 250 K, slightly above the transition temperature (T_{Film}) of the Ca_2RuO_4 film and below the transition temperature of the bulk Ca_2RuO_4 (T_{Bulk}). The colors and numbers mark the clusters of pixels on the detector with correlated patterns in real space (raster maps). The translation of class information onto the diffraction pattern (Figure 3a) yields intuitive and discrete regions. Clusters 1 and 2 are positioned along the diagonal and off-center. These clusters are associated with satellite peaks visible in XRD (see Figure S5, Supporting Information) and identify the structure that emerges at low temperatures. Clusters 3 and 4 encompass areas of the highest relative intensity in the center of the diffraction pattern, likely connected to a high-temperature structure as the center peak is present at 300 K (see Figure S7, Supporting Information). Cluster 5 represents a diffuse halo around the center peak. Similar data has been linked to diffuse scattering emerging from localized strain regions due to crystal defects.[22] Despite low signal per pixel in individual diffraction patterns, the total signal in every cluster for individual diffraction patterns is on the order of and above 100 photons, which makes it possible to create corresponding maps of the structure in the film for every cluster.

Maps of the corresponding structural phase distribution (Figure 3b) show the domains of the structural phases in the film. The maps were obtained by calculating the total intensity within the corresponding cluster as a function of the position on the film. A subset of maps, corresponding to correlated clusters 1

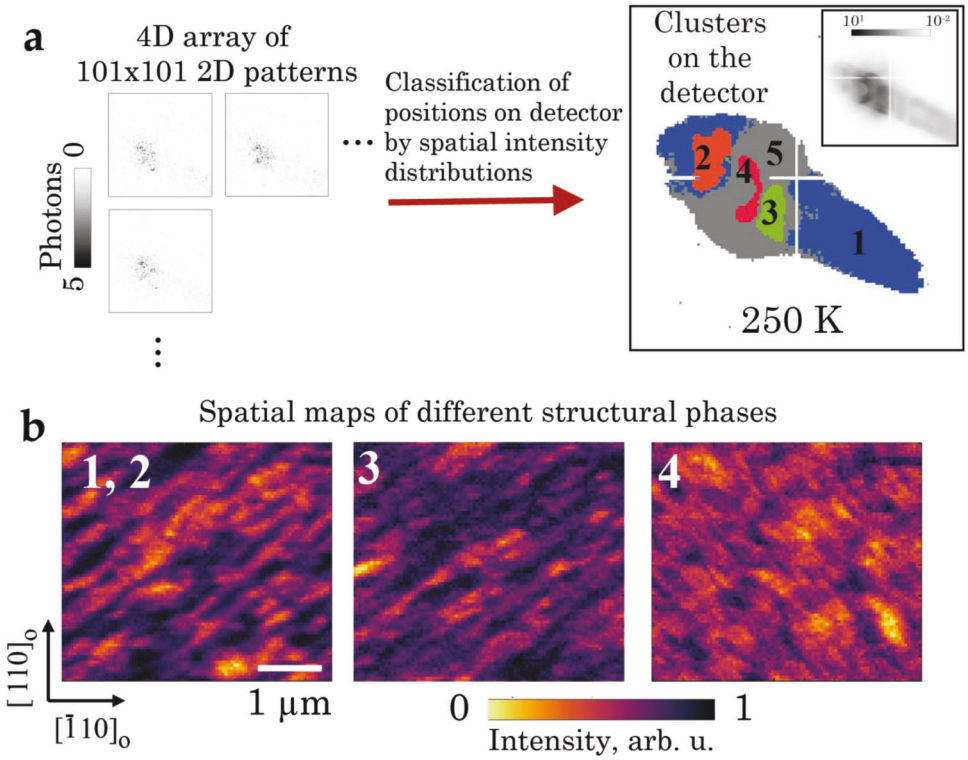

Figure 3. Classification of the diffraction pattern regions and corresponding structural maps. a) A 4D array of intensities as a function of position in real space (on the film) and on the diffraction pattern is processed through a k-means classification algorithm to determine regions of the diffraction pattern corresponding to distinct heterogeneities in the real space. b) Real space intensity maps corresponding to different clusters: 1,2 –structure associated with regions of the diffraction pattern only present at or below transition temperature; 3 – "high-temperature phase" structure, anticorrelated to 1,2; 4 – structure only present at or above transition temperature.

and 2 and cluster 3, exhibit characteristic diagonal stripes hundreds of nm in size oriented along the orthorhombic $[010]_o$ crystallographic direction. The maps for clusters 1+2 and 3 display a degree of anticorrelation, suggesting competing phases and showing domain separation in real space, similar to other Mott insulators.[27] Unexpectedly, the spatial map of cluster 4 presents an alternative stripe orientation, oriented along $[100]_o$ direction, that is, orthogonal to phase distribution domains. The data collected at 250 K demonstrates that the system hosts three distinct structures near the MIT temperature: A – a nanotextured phase with a distribution shown in Figure 3b (clusters 1 and 2), B – an anticorrelated nanotextured phase with a distribution shown in Figure 3b (cluster 3), and C – a third structure shown in Figure 3b (cluster 4) with diagonal stripes oriented orthogonally to the stripes observed in structure (A) and (B).

We performed in situ X-ray nanodiffraction at different temperatures through the phase transition to elucidate the development and nature of the strain modulation morphology. **Figure 4** shows maps for combined clusters 1 and 2 for different temperatures on a heating and cooling branch. On the heating branch, maps at 110 and 250 K show evolving features; such features are also observed on the cooling branch. After a heating and cooling cycle, the film does not reform in the exact same configuration, as evidenced by the difference in maps on the heating branch and on the cooling branch at similar temperatures (see cross-correlation between the maps in Figure S10, Supporting Information), meaning that the domain formation mechanism is intrinsic and the domain pinning by structural defects is weak. Fourier transform of a spatial map projection at 250 K onto the diagonal shown by a blue dashed line shows a periodicity of 250 nm present in the structure (Figure 4b). Note that the static domain size is similar to that observed on the surface of bulk crystals in experiments with applied current,[15] hinting at an intrinsic length scale in the material present in bulk and thin films. The domains at lower temperatures have a stripe shape with a preferential orientation; however, on the cooling branch, it is visible in the 240 K domain map that the domains start as "pools". It was previously observed in ruthenates under external stress that structural phase domains tend to grow fastest in the direction of the maximum stress,[28] and a different striped structure on the surface of bulk Ca_2RuO_4 in[15] was also connected to the stress direction. In the strained film that we measured, the direction of the maximal stress coming from the substrate is the $[010]_o$ direction,[12] which would be oriented at 45° to the edges of the measured square region.

At 300 K, the clustering reveals that the "medium-scale" (MS), high-temperature structure visible in cluster 4 at 250 K persists despite the absence of a satellite streak associated with the low-temperature phase domains. The MS structure is not visible at temperatures below 200 K. In short, the low-temperature 250 nm stripe structure is only present at or below T_{Film}, while a perpendicular MS stripe structure is only present at or above T_{Film}.

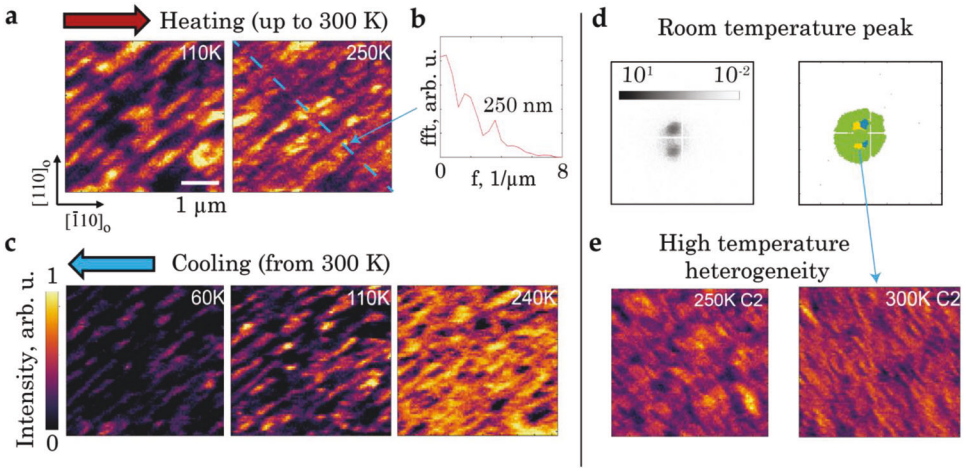

Figure 4. Phase distribution as a function of temperature. a) Maps of the structural heterogeneity in the same region of the film at different temperatures at the heating branch, the heterogeneity corresponding to clusters 1,2 in Figure 3. b) Fourier transform of the spatial map projection on the blue dashed line. c) Maps of the structural heterogeneity in the same film region for the cooling branch. The domain pattern for the cooling branch is notably different from the heating branch due to both the intrinsic nature of the pattern and hysteresis. d) Regions of the room temperature (300 K) diffraction pattern marked according to classification results for that temperature (inset – average over diffraction patterns) and defects visible in the diffuse scattering.[22] e) Maps of the phase distribution of the second structure corresponding to the "yellow" (left) cluster in (d) at room temperature and cluster (4) in Figure 3.

We studied the impact of the supercrystal pattern on electric transport by measuring the local resistivity anisotropy through the MIT by using microscale devices (see Figure 1b; Figures S2–S4, Supporting Information). When the resistivity is measured along two orthogonal crystallographic directions $[100]_o$ and $[010]_o$, the conductivity is higher along $[010]_o$ by a factor of ≈3 at room temperature. The direction of the lowest resistivity changes from $[010]_o$ by 90° to $[100]_o$ when cooled through the MIT. At the nanoscale, therefore, the structural and electronic anisotropy appear to strongly correlate. Our X-ray measurements demonstrate, therefore, an anistropic structural inhomogeneity, its intrinsic nature, the switching of anisotropy direction, and its correlation with the anisotropy of electrical resistivity we found through local measurements of electronic transport.

3. Fine-Scale Domain Structure: Characterization and Theory

To better characterize the 30 nm periodic structure, we collected synchrotron XRD measurements on a 35 nm thick Ca_2RuO_4 film with a 500 μm large parallel beam. The data demonstrate a Bragg peak shape markedly different from bulk observations (Figure S5, Supporting Information; similar to a 17 nm film in ref. [13]). At a temperature of T = 300 K ($T_{Film} < T < T_{Bulk}$), the diffraction pattern does not consist of a single Bragg peak. Rather it is twinned due to a tens-of-microns-sized twin-domain structure imposed on the film by the $LaAlO_3$.[29] Below T_{Film} additional satellite peaks around each twin-peak are present. The observed diffraction pattern is reminiscent of the Bragg peaks typically found in ferroelectric thin films caused by a herringbone twin domain structure (see, e.g., Figure 9c in ref. [30] or Figure 3 in ref. [31]). The satellite peak orientation that we observed suggests a herringbone pattern oriented out of the film plane. The distance between the fringes of the satellite streaks indicates the average nanotexture domain size of ≈30 nm projected on the film surface (larger than in a thinner film reported in ref. [13]). To directly investigate the atomic structure associated with a herringbone-like domain pattern at low temperatures, we performed temperature-dependent STEM measurements finding a herringbone-like domain structure when the film is viewed in cross section along the zone axis at cryogenic temperatures below T_{film}, and a homogeneous structure at room temperature (**Figure 5a**).

To further explain the fine-scale domain structure formed during the transition, a computational approach was adopted. Following Khachaturyan's microelasticity theory,[32] we investigated the favorable interface directions between *S-Pbca* and *L-Pbca* phases, which minimizes the elastic free energy. Given the lattice parameters for the *S-Pbca* phase (a_S = 5.60 Å, b_S = 5.39 Å, c_S = 11.76 Å) and the *L-Pbca* phase (a_L = 5.36 Å, b_L = 5.35 Å, c_L = 12.26 Å), the favored interface normal directions will be close to $[021]_o$ and $[02\bar{1}]_o$, with a 48° tilting angle measured from the $\{001\}_o$ plane as shown in Figure 5b, which is consistent with the diffraction patterns and the STEM images. To further elucidate the pattern observed on the cross-sectional image of the film, we used the phase-field method to simulate the *L-Pbca/S-Pbca* structure.[33,34] With a −1.6% epitaxial strain applied on a 34 nm-thick film cross section (taking the *L-Pbca* phase as the reference), the result of the temporal relaxation from a random initial structure is shown in Figure 5c. In the plot, an order parameter u is used to distinguish between the phases. The plot shows tilted stripes in two directions formed with the coexistence of L/S phases, with a ≈30 nm periodicity, which agrees with the experimental observations. The stripes' tilting angle is close to the microelasticity predictions, which suggests that the formation of the nanostructures is a result of the minimization of the elastic free energy. We also investigated the change in the lattice parameter along the *c*-axis of the orthorhombic structure, by computing $c = c_L(1 + \epsilon_{33})$, where ϵ_{33} is the out-of-plane normal strain component. The results depicted in Figure 5d show a distortion along the *c* axis, which corresponds to the change in

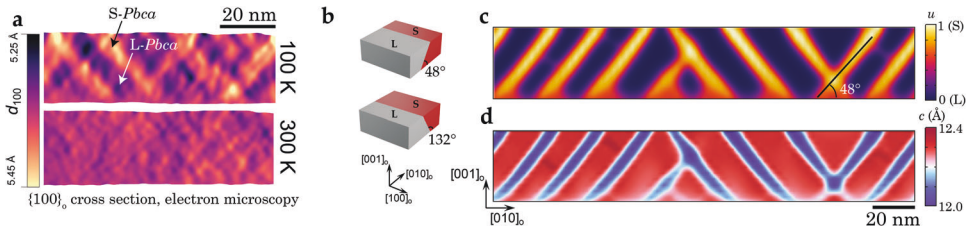

Figure 5. Electron microscopy and mechanical model. a) Real space maps of the (010) inter-planar spacing (d_{010}) extracted from STEM images of a cross-section of the film on the [100] zone axis (unprocessed images in Figure S1, Supporting Information). b) Prediction of the favored interface directions according to microelasticity theory. c) Distribution of order parameter u in the $\{100\}_o$ cross section. $u = 0$ stands for *S-Pbca* phase and $u = 1$ for *L-Pbca* phase. d) The map of lattice parameter c in the cross section obtained by $c = c_L(1 + \epsilon_{33})$.

interplanar distances as observed using HAADF-STEM and the diffraction streak in the nanodiffraction data.

In order to confirm the qualitative correspondence of the fine-scale domain structure at different temperatures, we performed measurements of 3D X-ray Bragg peaks with a wide, 500 µm beam at different temperatures (Figure S5, Supporting Information). Satellite diffraction peaks corresponding to the periodicity of the fine-scale domain structure are present through and below the transition temperature, as seen in Figure S5a,b (Supporting Information), and absent above (Figure S5c, Supporting Information). The direction of the "streak" in X-ray nanodiffraction patterns corresponds to one of the streaks in the wide-beam diffraction pattern. The cryo-STEM, microelasticity model, and conventional reciprocal space mapping allow us to determine that in Figures 3, 4, clusters 1 and 2 originate from regions containing the fine-scale domain strucutre, while cluster 3 originates from regions lacking fine-scale domain structure.

4. Discussion

We found a stable, oriented, and periodic structural heterogeneity – a supercrystal – arising intrinsically in a strained Ca_2RuO_4 film, observed switching of the structure anisotropy around MIT temperature, and further found switching of electronic resistivity anisotropy, that we demonstrate correlates to the switching in structural anisotropy. We provide a self-consistent scheme of the total structure below MIT temperature T_{film} presented in Figure 1 based on our combined measurements and the comparative (perpendicular) orientation of the streaks in the x-ray diffraction data produced by the fine-scale (30 nm) domain structure to the coarse-scale (250 nm) domain structure. Below T_{film}, the coarse-scale nanotexture is oriented along the $[010]_o$ direction, and a fine-scale herringbone-like structure is folded within the stripes of the larger nanotexture (Figure 1a). At high temperatures, a different coarse-scale structural morphology is found, with stripes of a different crystal lattice period and unclear origin oriented along $[100]_o$ – perpendicular to the low-temperature coarse-scale structure. We hypothesize that the stripes at room temperature appear due to elastic frustration – the temperature is lower than the bulk MIT temperature – producing a strained superstructure. The two structural morphologies coexist around the film MIT temperature of ≈250 K. During cooling, the disappearance of high-temperature morphology and appearance of low-temperature supercrystal results in an apparent rotation of the stripes. We found that the direction of the preferential local electronic transport correlates to the orientation of the stripes comprising the ≈250 nm periodicity order of the supercrystal. The correlation between structure and conductivity suggests that the stripes of the conducting phase are responsible for the variation in the transport direction. Dynamical mean-field theory indicates that in Ca_2RuO_4, the Mott transition is locally driven by the change in the structure.[9] The coincident rotation of the structural stripes and the easy axis in anisotropic transport, as presented here, suggests that the structure of the supercrystal also governs the larger-scale direction of electron flow.

Our findings are particularly significant in the context of multiple recent studies of moiré patterns/superlattices that achieved previously unreachable electronic, photonic, magnetic, and topological functionalities in 2D materials.[3,35–38] Similarly, induced supercrystals could potentially expand the palette of achievable properties in thin films. Our research shows how strain can be employed to manipulate supercrystals in thin films. Furthermore, the existence of metastable superlattices photoinduced in heterostructures[1] suggests a potential complex ultrafast behavior of the supercrystal, as well as the potential for further tuning the physical properties of the supercrystal phase by combining multiple layers of Ca_2RuO_4 films in a heterostructure.

In our multimodal measurements combining X-ray, electron microscopy, and transport measurements with microscopic devices, X-ray Bragg nanodiffraction provides a unique perspective on the structure of the film. It directly couples to lattice distortions and typically generates real-space maps of heterogeneities in the film-plane. Complementary electron microscopy provides atomistic insight into the cross-sectional structure of the film due to the projection nature of the technique and its constraint to thin flakes extracted perpendicular to the film surface. The two techniques also differ in the length scales at which they offer the greatest structural information: electron microscopy provides the atomic resolution necessary to characterize the fine stripe structure shown in Figure 5a but currently it cannot reasonably be extended to the 5 × 5 µm^2 areas used to visualize the distinct large scale stripe texture shown in Figures 2–4. Nanodiffraction provides access to larger areas yet is limited in resolution to a few tens of nanometers. As such, electron microscopy detects the fine-scale domain structure (30 nm) in the cross-cut, but not the higher level of the hierarchy (250 nm) in the plane of the film. The larger anisotropic domain patterns observed by X-ray nanodiffraction at low and high temperatures are the anisotropic heterogeneity we correlate to the directional electronic properties. The larger-scale X-ray observations therefore let us make the link between the structural and electronic properties. To summarize, combining cryo-STEM and cryo-nanodiffraction was

critical for constructing a structural model of the supercrystal with various levels of hierarchy emerging below and above the metal-to-insulator transition temperature. As an outlook, X-ray nanodiffraction provides the potential to perform operando current measurements in full devices, and the high coherence of X-ray nanobeams provides an opportunity for correlative and statistical measurements over a large range of areas and timescales.

While our data leaves some structural ambiguities, future advancements in spatially resolved electronic measurements, x-ray methods, and machine learning might provide further clarity. From our data, we cannot distinguish between the two possible orthogonal relative orientations of electronic transport and supercrystal order or resolve electronic transport on a nanometer length scale. This question might be further clarified by spatially resolved electronic measurements, for example, SNOM.[15] The exact distribution of the underlying 30 nm domain structure within the larger 250 nm stripes within the film cannot be resolved with currently available diffraction methods which allow multiple possible constructions of a supercrystal from available data similar to the one presented in Figure 1a. With advances in x-ray sources,[39] nanodiffraction will likely be able to resolve the underlying fine-scale domain structure directly within the larger domains. X-ray spectroscopy at a nanoscale would also be available on the new sources, which could provide complementary electronic information. In parallel, recent advances in variable-temperature cryo-STEM[18,19] may also provide access to map the interplay between the fine 30 nm structure and the larger 250 nm domains at controlled temperatures. Machine learning approaches for multiscale hierarchical structures will be useful to further identify structures with better spatial and especially temporal resolution, using, for example, additional limitations on input.[40]

The new hierarchies of periodicity presented here highlight prospects for inducing novel properties in nanomaterials. In particular, the impact of the superstructure on the preferential transport direction offers compelling opportunities for controlling electronic properties. The switchable behavior of the transport direction, modifiable by temperature changes, is especially intriguing for electronic and mottronic applications. Our work showcases a rotation of transport anisotropy in response to temperature modulation. Another potential avenue for investigation would be the possibility of rotation of structural order by the application of current[41] or light. Our initial attempts to rotate the direction of the easy resistivity axis by current were unsuccessful, suggesting a large energy barrier for the 250 nm stripe rotation. Finally, the 30 nm herringbone-like phase distribution significantly expands the surface area, presenting opportunities for interface physics. The supercrystal hierarchies and their potential effects on nanomaterial physical properties, especially in electronic applications, are promising areas for further exploration.

5. Experimental Section

Sample Preparation: A Ca_2RuO_4 thin film ≈34 nm thick was grown in a Veeco Gen10 molecular-beam epitaxy system on a $(001)_{pc}$-oriented $LaAlO_3$ substrate from CrysTec GmbH, where pc denotes pseudocubic indices. The film was grown at a substrate temperature of 870 °C as measured using a pyrometer operating at 1550 nm. Elemental calcium (99.99% purity) and elemental ruthenium (99.99% purity) were evaporated from a low-temperature effusion cell and an electron beam evaporator, respectively. The films were grown with a calcium flux of 1.8×10^{13} atoms $cm^{-2}\,s^{-1}$ and a ruthenium flux of 1.7×10^{13} atoms $cm^{-2}\,s^{-1}$ in a background pressure of 7×10^{-7} Torr of ozone (10% O_3 + 90% O_2). At the end of the growth, the shutters on both the calcium and ruthenium sources were closed, and the sample was cooled down to 250 °C in the same background pressure of ozone as used during the growth. All data presented in this paper were collected on the same film.

Electron Microscopy: Scanning transmission electron microscopy (STEM) measurements were performed on a cross-sectional lamella prepared via focused ion beam (FIB) lift-out with a Thermo Fisher Helios G4 UX FIB. Cryogenic and room temperature high-angle annular dark-field (HAADF) STEM imaging were performed sequentially on the same day on an FEI/Thermo Fisher Titan Themis 300 CryoS/TEM with a Gatan 636 double tilt liquid nitrogen cooling holder operating at 300 kV with a 30 mrad probe convergence semi-angle. For high-precision structural measurements, a series of 20 rapid-frame images (≈1.6 sec. per frame) were acquired, aligned, and averaged by a method of rigid registration optimized to prevent lattice hops[42] to recover high signal-to-noise ratio, high fidelity atomic resolution images. The d_{100} interplanar spacing was extracted from the HAADF-STEM images using a strain mapping technique developed by Smeaton et al.[43] Unprocessed images and corresponding interplanar spacing maps are shown in Figure S1 (Supporting Information).

Device Fabrication and Local Resistivity Tensor Measurements: To measure the local in-plane resistivity tensor (over a 6-µm-wide region) of the (001)-oriented Ca_2RuO_4 thin film, regions of the sample were fabricated into Hall bars with a channel width of 6 µm along various directions as defined by photolithography, and Ar^+ ion milling. Pt/Ti pads were sputtered on the thin films to form Ohmic contacts. The resistivity tensor elements ρ_{xx}, ρ_{yy}, and ρ_{xy} were obtained from the longitudinal and transverse resistances of the Hall bars, which were measured in a Physical Property Measurement System (PPMS, Quantum Design, Inc.) The resistivity tensor $\rho_{ij}(T)$ was then diagonalized at each temperature to obtain two eigenvalues, a larger $\rho_{max}(T)$ and a smaller $\rho_{min}(T)$, as well as the angle $\alpha[\rho_{min}]$ between the eigenvector of $\rho_{min}(T)$ and the pseudocubic $[110]_{LAO}$ directions. A phase shift of $\alpha(T)$ by 90° was observed when the temperature of the sample crosses the metal-to-insulator transition.

X-Ray Measurements: All scanning X-ray nano-diffraction experiments were conducted at the 26 ID Hard X-ray Nanoprobe Beamline operated by the Center for Nanoscale Materials at the Advanced Photon Source, Argonne National Laboratory. A liquid helium cryostat was used to cool the samples. A liquid-nitrogen-cooled Si (111) double crystal monochromator gave energy resolution $\Delta E/E = 1.7 \times 10^{-4}$ and the x-ray photon energy of 10 keV. A Fresnel zone plate with an outside diameter of 150 µm and outermost zone width of 16 nm combined with an order sorting aperture was used to focus the collimated x-ray beam to 30 nm diameter with the flux of $\approx 10^9$ photons s^{-1}. The sample-to-detector distance was 750 mm. We used a medipix detector, pixel size 55 × 55 µm, 4 panels of 256 × 256 pixels each. In the horizontal scanning direction, the projection of the beam onto the sample was 30 nm/sin (θ), where θ is the angle of the incident beam (≈23.9° for the Ca_2RuO_4 008 reflection at 10 keV). The horizontal footprint of the beam was, therefore, ≈80 nm. Raster scans were collected within $LaAlO_3$ domains, which were on the order of 50 µm.

Machine Learning: The machine learning section consisted of two parts: PCA for visualization and verification of the clusterization (see also Figure S9, Supporting Information) and the clustering itself (see also Figure S8, Supporting Information). Pixels of the detector (binned by 2 in every direction) were "observations", thresholded by the minimum average intensity of 0.025 photons per pixel. Intensity as a function of position on the film served as a "feature" for every pixel. The number of observations was therefore the number of (binned) pixels, and the number of variables was the number of probing points on the film. K-means clustering was used on the full dataset for every temperature instead of the first few principal components produced by PCA, due to a relatively low amount of variance explained by the first principal components (the first

3 principal components only explain ≈10% of the variance). Such a low proportion was due to the high noisiness of the data due to low signal (1-2 photons average per pixel per pattern). For k-means clustering, 10 000 initiations with randomized initial positions of the centroids were used. The final result chosen after convergence of each initiation was the one with a minimum sum of squared Euclidean distances of observations to their closest centroid. Note that clustering had to be performed for every temperature separately, due to the changing contrast of the domain pattern in real space and the intrinsic nature of the domain pattern (making them uncorrelated between repeated transitions).

One-Sentence Summary: A hierarchical anisotropic supercrystal, which dictates electronic anisotropy, was reported in a thin film during a Mott metal–insulator transition.

Supporting Information

Supporting Information is available from the Wiley Online Library or from the author.

Acknowledgements

The work was primarily supported by the U.S. Department of Energy, Office of Science, Office of Basic Energy Sciences, under Contract No. DE-SC0019414 (H.N. and D.G.S. for thin film synthesis and characterization; L.M. and K.M.S. for fiducial fabrication, device fabrication, and transport measurements; O.Y.G., Z.S., and A.S. for x-ray measurements, analysis, and interpretation). This research was funded in part by the Gordon and Betty Moore Foundation's EPiQS Initiative through grant nos. GBMF3850 and GBMF9073 to Cornell University. Work performed at the Center for Nanoscale Materials and Advanced Photon Source, both U.S. Department of Energy Office of Science User Facilities, was supported by the U.S. DOE, Office of Basic Energy Sciences, under Contract No. DE-AC02-06CH11357. Device fabrication was, in part, facilitated by the Cornell NanoScale Facility, a member of the National Nanotechnology Coordinated Infrastructure (NNCI), which was supported by NSF Grant No. NNCI-2025233. Transmission electron microscopy work was supported by the National Science Foundation (Platform for the Accelerated Realization, Analysis, and Discovery of Interface Materials (PARADIM)) under Cooperative Agreement No. DMR-2039380 and made use of the Cornell Center for Materials Research Shared Facilities, which were supported through the NSF MRSEC program (DMR-1719875). N.S. was supported by the NSF Graduate Research Fellowship (DGE-2139899). B.H.G. was supported by PARADIM (NSF DMR-2039380). K.M.S. and L.M. acknowledge support from the Air Force Office of Scientific Research Grant No. FA9550-21-1-0168 and the National Science Foundation DMR-2104427. L.F.K. acknowledges support by the Packard Foundation. Y.T. and L.Q.C.'s work was supported by the Penn State Center for Nanoscale Sciences, an NSF MRSEC under the grant number DMR-2011839 (2020 – 2026). L.Q.C. acknowledges new the U.S. Department of Energy, Office of Science, Office of Basic Energy Sciences, under Award Number DE-SC-0012375 for support studying complex-oxide heterostructure with X-ray scattering. The authors thank Dr. Sergey Antopolsky for useful discussions regarding machine learning algorithms.

Conflict of Interest

The authors declare no conflict of interest.

Data Availability Statement

The data that support the findings of this study are available from the corresponding author upon reasonable request. The scanning transmission electron microscopy data of the Ca_2RuO_4 thin film is available for download at the Platform for the Accelerated Realization, Analysis, and Discovery of Interface Materials database (PARADIM) (https://doi.org/10.34863/bkx0-ym97).

Keywords

coherent X-ray diffraction, nanomaterials, quantum materials, supercrystals, thin films

Received: March 15, 2024
Revised: June 4, 2024
Published online: June 27, 2024

[1] V. A. Stoica, N. Laanait, C. Dai, Z. Hong, Y. Yuan, Z. Zhang, S. Lei, M. R. McCarter, A. Yadav, A. R. Damodaran, S. Das, G. A. Stone, J. Karapetrova, D. A. Walko, X. Zhang, L. W. Martin, R. Ramesh, L.-Q. Chen, H. Wen, V. Gopalan, J. W. Freeland, *Nat. Mater.* **2019**, *18*, 377.
[2] M. Yankowitz, J. Xue, D. Cormode, J. D. Sanchez-Yamagishi, K. Watanabe, T. Taniguchi, P. Jarillo-Herrero, P. Jacquod, B. J. LeRoy, *Nat. Phys.* **2012**, *8*, 382.
[3] L. Du, M. R. Molas, Z. Huang, G. Zhang, F. Wang, Z. Sun, *Science* **2023**, *379*, 6639.
[4] Y. Tokura, M. Kawasaki, N. Nagaosa, *Nat. Phys.* **2017**, *13*, 1056.
[5] L. Pellegrino, N. Manca, T. Kanki, H. Tanaka, M. Biasotti, E. Bellingeri, A. S. Siri, D. Marré, *Adv. Mater.* **2012**, *24*, 2929.
[6] N. A. Butakov, I. Valmianski, T. Lewi, C. Urban, Z. Ren, A. A. Mikhailovsky, S. D. Wilson, I. K. Schuller, J. A. Schuller, *ACS Photonics* **2017**, *5*, 371.
[7] J. Lin, S. Guha, S. Ramanathan, *Front. Neurosci.* **2018**, *12*, 11.
[8] C. S. Alexander, G. Cao, V. Dobrosavljevic, S. McCall, J. E. Crow, E. Lochner, R. Guertin, *Phys. Rev. B* **1999**, *60*, R8422.
[9] E. Gorelov, M. Karolak, T. O. Wehling, F. Lechermann, A. I. Lichtenstein, E. Pavarini, *Phys. Rev. Lett.* **2010**, *104*, 6.
[10] C. Dietl, S. K. Sinha, G. Christiani, Y. Khaydukov, T. Keller, D. Putzky, S. Ibrahimkutty, Wochner, G. Logvenov, A. van Aken, B. J. Kim, B. Keimer, *Appl. Phys. Lett.* **2018**, *112*, 031902.
[11] L. Miao, W. Zhang, Silwal, X. Zhou, I. Stern, T. Liu, J. Peng, J. Hu, D. H. Kim, Z. Q. Mao, *Phys. Rev. B* **2013**, *88*, 9.
[12] O. Friedt, M. Braden, G. ré Adelmann, S. Nakatsuji, Y. Maeno, *Phys. Rev. B* **2001**, *63*, 4.
[13] Z. Shao, N. Schnitzer, J. Ruf, O. Y. Gorobtsov, C. Dai, B. H. Goodge, T. Yang, H. Nair, V. A. Stoica, J. W. Freeland, J. Ruff, L.-Q. Chen, D. G. Schlom, K. M. Shen, L. F. Kourkoutis, A. Singer, *Proc. Natl. Acad. Sci. U. S. A.* **2023**, *120*.
[14] F. Nakamura, M. Sakaki, Y. Yamanaka, S. Tamaru, T. Suzuki, Y. Maeno, *Sci. Rep.* **2013**, *3*, 8.
[15] J. Zhang, A. S. McLeod, Q. Han, X. Chen, H. A. Bechtel, Z. Yao, S. G. Corder, T. Ciavatti, T. H. Tao, M. Aronson, G. Carr, M. C. Martin, C. Sow, S. Yonezawa, F. Nakamura, I. Terasaki, D. Basov, A. J. Millis, Y. Maeno, M. Liu, *Phys. Rev. X* **2019**, *9*, 2.
[16] J. Bertinshaw, N. Gurung, Jorba, H. Liu, M. Schmid, D. Mantadakis, M. Daghofer, M. Krautloher, A. Jain, G. Ryu, O. Fabelo, Hansmann, G. Khaliullin, C. Pfleiderer, B. Keimer, B. Kim, *Phys. Rev. Lett.* **2019**, *123*, 9.
[17] K. Jenni, F. Wirth, K. Dietrich, L. Berger, Y. Sidis, S. Kunkemöller, C. Grams, D. I. Khomskii, J. Hemberger, M. Braden, *Phys. Rev. Mater.* **2020**, *4*, 8.
[18] B. H. Goodge, E. Bianco, N. Schnitzer, H. W. Zandbergen, L. F. Kourkoutis, *Microsc. Microanal.* **2020**, *26*, 439.
[19] N. Schnitzer, B. H. Goodge, G. Powers, J. Kim, S.-W. Cheong, I. E. Baggari, L. F. Kourkoutis, "Tracking topological defect motion, incommensurate charge order melting in a perovskite manganite", *Preprint*, **2024**, arXiv:2402.08580.
[20] R. Winarski, M. V. Holt, V. Rose, Fuesz, D. Carbaugh, C. Benson, D. Shu, D. Kline, G. B. Stephenson, I. McNulty, J. Maser, *J. Synchrotron. Radiat.* **2012**, *19*, 1056.

[21] S. O. Hruszkewycz, M. V. Holt, J. Maser, C. E. Murray, M. J. Highland, C. M. Folkman, H. Fuoss, *Philos. Trans. R. Soc., A* **2014**, *372*, 20130118.
[22] A. Luo, O. Y. Gorobtsov, J. N. Nelson, D.-Y. Kuo, T. Zhou, Z. Shao, R. Bouck, M. J. Cherukara, M. V. Holt, K. M. Shen, D. G. Schlom, J. Suntivich, A. Singer, *Appl. Phys. Lett.* **2022**, *121*, 43153904.
[23] I. T. Jolliffe, *Principal Component Analysis*, Springer-Verlag GmbH, Berlin, Germany, **2002**.
[24] I. T. Jolliffe, J. Cadima, *Philos. Trans. R. Soc., A* **2016**, *374*, 20150202.
[25] H. Abdi, L. J. Williams, *Wiley Interdiscip. Rev.: Comput. Stat.* **2010**, *2*, 433.
[26] S. Lloyd, *IEEE Trans. Inf Theory* **1982**, *28*, 129.
[27] A. Singer, J. G. Ramirez, I. Valmianski, D. Cela, N. Hua, R. Kukreja, J. Wingert, O. Kovalchuk, J. M. Glownia, M. Sikorski, M. Chollet, M. Holt, I. K. Schuller, O. G. Shpyrko, *Phys. Rev. Lett.* **2018**, *120*, 207601.
[28] T.-H. Kim, M. Angst, B. Hu, R. Jin, X.-G. Zhang, J. F. Wendelken, E. W. Plummer, A. Li, *Proc. Natl. Acad. Sci. U. S. A.* **2010**, *107*, 5272.
[29] S. Bueble, K. Knorr, E. Brecht, W. W. Schmahl, *Surf. Sci.* **1998**, *400*, 345.
[30] J. Schwarzkopf, D. Braun, M. Hanke, R. Uecker, M. Schmidbauer, *Front. Mater.* **2017**, *4*, 8.
[31] M. Schmidbauer, D. Braun, T. Markurt, M. Hanke, J. Schwarzkopf, *Nanotechnology* **2017**, *28*, 24LT02.
[32] A. G. Kačaturjan, Theory of structural transformations in solids, Dover ed., 1. publ., unabridged republ. ed., Dover Publications, Mineola, NY, **2008**.
[33] L. Q. Chen, J. Shen, *Comput. Phys. Commun.* **1998**, *108*, 147.
[34] L.-Q. Chen, Y. Zhao, *Prog. Mater. Sci.* **2022**, *124*, 100868.
[35] C. Jin, Z. Tao, T. Li, Y. Xu, Y. Tang, J. Zhu, S. Liu, K. Watanabe, T. Taniguchi, J. C. Hone, L. Fu, J. Shan, K. F. Mak, *Nat. Mater.* **2021**, *20*, 940.
[36] E. C. Regan, D. Wang, C. Jin, M. I. B. Utama, B. Gao, X. Wei, S. Zhao, W. Zhao, Z. Zhang, K. Yumigeta, M. Blei, J. D. Carlström, K. Watanabe, T. Taniguchi, S. Tongay, M. Crommie, A. Zettl, F. Wang, *Nature* **2020**, *579*, 359.
[37] K. L. Seyler, Rivera, H. Yu, N. Wilson, E. L. Ray, D. G. Mandrus, J. Yan, W. Yao, X. Xu, *Nature* **2019**, *567*, 66.
[38] A. L. Sharpe, E. J. Fox, A. W. Barnard, J. Finney, K. Watanabe, T. Taniguchi, M. A. Kastner, D. Goldhaber-Gordon, *Science* **2019**, *365*, 605.
[39] P. Raimondi, C. Benabderrahmane, P. Berkvens, J. C. Biasci, Borowiec, J.-F. Bouteille, T. Brochard, N. B. Brookes, N. Carmignani, L. R. Carver, J.-M. Chaize, J. Chavanne, S. Checchia, Y. Chushkin, F. Cianciosi, M. D. Michiel, R. Dimper, A. D'Elia, D. Einfeld, F. Ewald, L. Farvacque, L. Goirand, L. Hardy, J. Jacob, L. Jolly, M. Krisch, G. L. Bec, I. Leconte, S. M. Liuzzo, C. Maccarrone, et al., *Commun. Phys.* **2023**, *6*, 82.
[40] C. M. Heil, Y. Ma, B. Bharti, A. Jayaraman, *JACS Au* **2023**, *3*, 889.
[41] L. Caretta, Y.-T. Shao, J. Yu, A. B. Mei, B. F. Grosso, C. Dai, Behera, D. Lee, M. McCarter, E. Parsonnet, K. P. Harikrishnan, F. Xue, X. Guo, E. S. Barnard, S. Ganschow, Z. Hong, A. Raja, L. W. Martin, L.-Q. Chen, M. Fiebig, K. Lai, N. A. Spaldin, D. A. Muller, D. G. Schlom, R. Ramesh, *Nat. Mater.* **2022**, *22*, 207.
[42] B. H. Savitzky, I. E. Baggari, C. B. Clement, E. Waite, B. H. Goodge, D. J. Baek, J. Sheckelton, C. Pasco, H. Nair, N. J. Schreiber, J. Hoffman, A. S. Admasu, J. Kim, S.-W. Cheong, A. Bhattacharya, D. G. Schlom, T. M. McQueen, R. Hovden, L. F. Kourkoutis, *Ultramicroscopy* **2018**, *191*, 56.
[43] M. A. Smeaton, I. E. Baggari, D. M. Balazs, T. Hanrath, L. F. Kourkoutis, *ACS Nano* **2021**, *15*, 719.